





OATAO is an open access repository that collects the work of Toulouse researchers and makes it freely available over the web where possible

This is an author's version published in: <http://oatao.univ-toulouse.fr/27629>

**Official URL:**

<https://doi.org/10.1088/1757-899X/529/1/012008>

**To cite this version:**

Marin, Raphaël  and Combeau, Hervé and Zollinger, Julien and Dehmas, Moukrane  and Rouat, Bernard and Lamontagne, Aude and Cardinaux, David and Lhenry-Robert, Lucile *Solidification path and phase transformation in super-austenitic stainless steel UNS S31254*. (2019) IOP Conference Series: Materials Science and Engineering, 529. 1-6. ISSN 1757-899X

Any correspondence concerning this service should be sent to the repository administrator: [tech-oatao@listes-diff.inp-toulouse.fr](mailto:tech-oatao@listes-diff.inp-toulouse.fr)

PAPER • OPEN ACCESS

## Solidification path and phase transformation in super-austenitic stainless steel UNS S31254

To cite this article: Raphaël Marin *et al* 2019 *IOP Conf. Ser.: Mater. Sci. Eng.* **529** 012008

View the [article online](#) for updates and enhancements.



**240th ECS Meeting** ORLANDO, FL

Orange County Convention Center **Oct 10-14, 2021**



Abstract submission due: April 9

**SUBMIT NOW**

# Solidification path and phase transformation in super-austenitic stainless steel UNS S31254

Raphaël Marin<sup>1,2,3</sup>, Hervé Combeau<sup>1</sup>, Julien Zollinger<sup>1</sup>, Moukrane Dehmas<sup>2</sup>, Bernard Rouat<sup>1</sup>, Aude Lamontagne<sup>3</sup>, David Cardinaux<sup>3</sup>, Lucile Lhenry-Robert<sup>3</sup>

<sup>1</sup> Université de Lorraine, CNRS, IJL, F-54000 Nancy, France;

<sup>2</sup> CIRIMAT, Université de Toulouse, CNRS, Toulouse, France;

<sup>3</sup> Industeel, Centre de Recherche des Matériaux du Creusot (CRMC), 71200 Le Creusot, France;

Raphaël Marin, [raphael.marin@univ-lorraine.fr](mailto:raphael.marin@univ-lorraine.fr)

**Abstract.** The solidification path and the  $\sigma$ -phase precipitation mechanism of UNS S31254 alloy were studied on the basis of directional solidified experiments accompanied by scanning electron microscopy observations and energy dispersive X-ray analysis. The resulting temperatures of solidification paths and phase transformation were compared with Gulliver-Scheil and equilibrium calculations predicted using ThermoCalc<sup>®</sup> software. It was confirmed that the experimental solidification path was in agreement with the thermodynamic calculations. The complementarity of the results have made it possible to propose a solidification path and a  $\sigma$ -phase precipitation mechanism for the UNS31254 steel.

## 1. Introduction

Stainless steels are an important class of materials. They are used everywhere, from daily life applications as cooking utensils to space vehicles. These steels are rich in chromium in order to get an oxide layer on the surface, which acts as protection against rusting and pitting. However, most of the stainless steels that are used in applications as seawater desalination and paper manufacturing plants require a better corrosion resistance [1–3]. Consequently, molybdenum is added to enhance corrosion resistance. During the processing route, the high amount of alloying elements contained in these steels can lead to the formation of chromium and molybdenum rich intermetallic precipitates and therefore to a significant lower corrosion resistance by removing these elements from the matrix. Especially, as-cast ingots exhibit  $\sigma$ -phase (space group 136, tetragonal [4]) in interdendritic region, that has to be eliminated by heat treatments after solidification. Numerous studies in the literature were focused on the  $\sigma$ -phase formation during heat treatment of different classes of stainless steels (ferritic, austenitic, duplex). There are two well established  $\sigma$ -phase precipitation mechanisms: (i)  $\sigma$ -phase nucleation in austenite [5–9], (ii)  $\sigma$ -phase nucleation due to the eutectoid decomposition of the  $\delta$ -ferrite [5,7,10–13]. However, to our knowledge, few studies report on the  $\sigma$ -phase precipitation mechanism during the solidification stage, especially in the S31254 (UNS norm) super-austenitic stainless steel (“super” = steel containing  $\approx$  50 wt.% iron – 50wt.% alloying elements [5]). Two cases are formulated in the literature for the  $\sigma$ -phase nucleation in cast stainless steel ingots; (i) it can be formed during the last stage of solidification due to the enrichment of the liquid in  $\sigma$ -forming elements [14], (ii) the interdendritic regions are composed of  $\delta$ -ferrite that decomposes through a solid-state phase transformation [15]. Both of these two hypotheses are related to the segregation of the molybdenum in the liquid during the solidification process [16].



This consideration prompted the present study that is focused on the study of the solidification path and the phases transformations of the UNS S31254 steel. A quenching directional solidification (QDS) set-up was used in parallel with ThermoCalc<sup>®</sup> simulations to establish the solidification path and the  $\sigma$ -phase transformation mechanism of the steel.

## 2. Material and experimental procedures

### 2.1. Material

The used steel was hot rolled grade, namely S31254 (UNS designation) and provided by INDUSTEEL company. The nominal chemical composition (wt.%) is given in Table 1.

**Table 1** – Nominal chemical composition of the S31254 steel in weight percent.

	Fe	Cr	Ni	Mo	Cu	Mn	Si	N
S31254	bal.	19.68	17.77	6.08	0.67	0.65	0.20	0.19

The equilibrium liquidus and solidus temperatures of the S31254 steel were determined using a Setaram multi detector high temperature calorimeter apparatus. In this way, various heating rates were applied (2, 5, 10°C/min). The equilibrium liquidus and solidus temperatures were found to be 1413°C and 1376°C respectively.

### 2.2. Quenching during Directional Solidification

Experiments involving Quenching during Directional Solidification (QDS) were performed with a specially designed Bridgman type furnace as previously described by Lacaze and Lesoult [17]. These experiments are achieved under argon gas flow. The samples were electromachined into cylindrical rods, 5 mm in diameter and 200 mm in length. They were introduced in an alumina tube of 5-mm inner diameter. The thermal history of the sample during the experiment was recorded by a Pt/Rh B-type thermocouple, which is located inside the sample and protected by an alumina tube. The directional solidification is achieved by pulling the alumina tube and the sample along the vertical axis at a constant solidification velocity ( $V = 5.10^{-5}$  m/s). The solidification velocity was chosen in order to have a directional solidification and not a longitudinal solidification. The thermal gradient,  $G$ , is controlled by the temperature difference between the inductive heater and the cooling box, which is filled with water. At constant solidification velocity,  $G$  controls the size of the mushy zone, *i.e.* the mushy zone. Once the major part of the sample is solidified, the sample is quenched by pulling it instantaneously through the cooling box in order to freeze the microstructure and the microsegregations. The induced cooling rate is close to 100°C/s (3.6.10<sup>5</sup>°C/h). This experiment enables to monitor separately the solidification velocity ( $V$ ) from the thermal gradient ( $G$ ). After the QDS experiments, the sample was polished along the longitudinal section, which is parallel to the growth direction. Each position in the sample corresponds to a given temperature of the steel before the quench at room temperature. In the present study, the average temperature gradient in the mushy zone was  $G=10000$ °C/m. The average cooling rate of the sample was calculated to be about 0.5°C/s (1800°C/h).

### 2.3. Microstructure analysis

The QDS samples were prepared using standard metallographic polishing. Final sample preparation was accomplished with colloidal silica. The microstructural observations were performed using a scanning electron microscopy (SEM) Quanta FEG 650 in backscattered electron mode (BSE), operated at an

acceleration voltage of 20Kv. Energy Dispersive X-ray (EDX) spectroscopy was used in order to analyse the elemental composition of the various phases.

### 3. Results and discussion

#### 3.1. Experimental solidification path and phase transformations

Figure 1 shows the solidification microstructure at the interface between the quenched liquid and the dendrites tip and the thermal history of the sample during the experiment. A deviation of  $15^{\circ}\text{C}$  on the temperature determination is considered due to the thermocouple accuracy and the repeatability. As shown in Figure 1.a, the interface between the quenched liquid and the dendrites tip is represented by the red dotted line. The dendrites grow along a direction close to the thermal gradient. Figure 1.b illustrates a part of the sample thermal history that was recorded during the experiment. These results were used to determine specific temperatures *i.e.* the liquidus temperature assuming the tip undercooling is negligible and the end of solidification. These particular temperatures were obtained with two tangential lines. The first line was draw to fit the thermal signal in the liquid, and the other one was fitting to the thermal signal obtained from the mushy zone. The intersection of these two tangential lines indicates the dendrites tip temperature. The same procedure was used to determine the end of solidification. The solidification starts at  $1430 \pm 15^{\circ}\text{C}$  and ends at  $1345 \pm 15^{\circ}\text{C}$ .

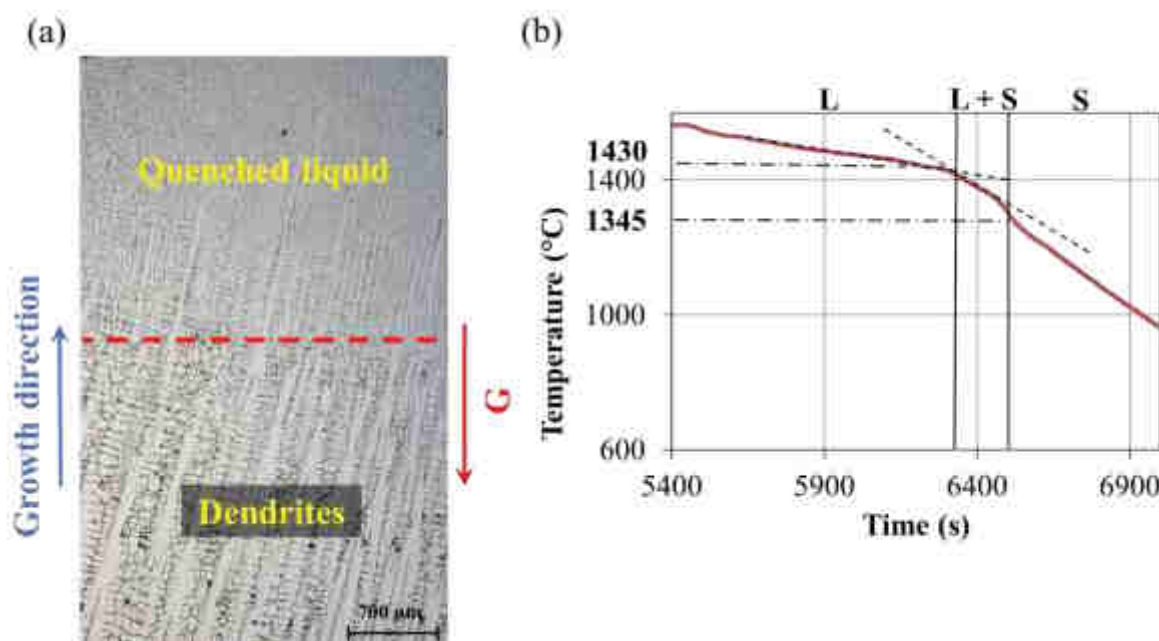
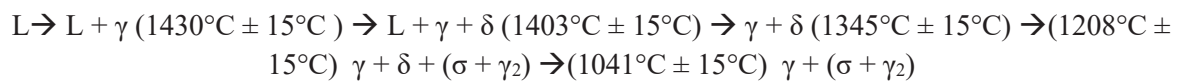


**Figure 1** – QDS results (a) QDS micrograph after NaOH (20%) + H<sub>2</sub>O (80%) electrolytic etching, 2.5 V, 5 seconds with the interface between the quenched liquid and the dendrites tip (red dotted line), (b) thermal history of the sample recorded by the thermocouple.

The microstructure evolutions during the solidification are reported with the corresponding temperatures on the Figure 2. The solidification starts at  $1430^{\circ}\text{C} \pm 15^{\circ}\text{C}$  with austenitic dendrites. At  $1403^{\circ}\text{C} \pm 15^{\circ}\text{C}$ , in the mushy zone, a new phase grow in the interdendritic spaces as shown in Figure 2.a. This phase should be  $\delta$ -ferrite due to the segregation of Mo in the liquid during the solidification [16]. Moreover, with the Cr, Ni and Mo content, the primary solidification is austenite while  $\delta$ -ferrite forms at a later stage[18]. The complete solidification occurs at  $1345 \pm 15^{\circ}\text{C}$ . At this temperature, the microstructure consists of austenite dendrites and  $\delta$ -ferrite in the interdendritic spaces. Thus, we can first conclude that no  $\sigma$ -phase was formed during the solidification period.

At lower temperature ( $1208^{\circ}\text{C} \pm 15^{\circ}\text{C}$ ), the solid-state transformation of interdendritic phase into two different phases occurs. As illustrated in Figure 2.b, the phase with a white grey level is enriched in Mo, Cr elements and depleted in Ni element, whereas the phase with a black grey level is enriched in Ni elements and depleted in Mo, Cr elements. These two phases seems to nucleate inside the  $\delta$ -ferrite grain. Numerous studies in the literature exhibit a similar microstructure and solid-state transformation in different types of stainless steel (duplex, ferritic) [10–13,19]. According to the literature and the SEM/EDS analysis that were performed, these phases can be identified as  $\sigma$ -phase and  $\gamma_2$  (eutectoid austenite). This transformation starts at  $1208^{\circ}\text{C} \pm 15^{\circ}\text{C}$  and ends at  $1041^{\circ}\text{C} \pm 15^{\circ}\text{C}$ . Below  $1041^{\circ}\text{C} \pm 15^{\circ}\text{C}$ , the  $\delta$ -ferrite is fully transformed into  $(\sigma + \gamma_2)$  and the microstructure is composed of austenite dendrites and  $(\sigma + \gamma_2)$  interdendritic precipitates, as shown in Figure 2.c.

Based on these assumptions, the solidification path and solid-state phase transformation of the S31254 steel can be expressed as following:



These results should be confirmed by further crystallographic analysis.

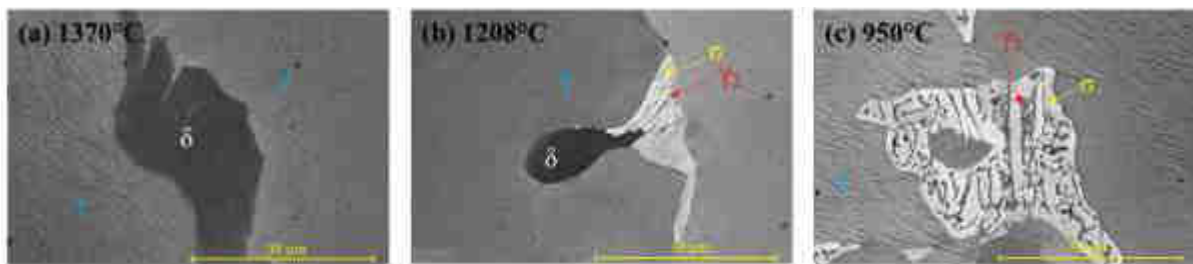


**Figure 2** – BSE micrographs of three different representative zones of the QDS sample : (a)  $1370^{\circ}\text{C} \pm 15^{\circ}\text{C}$ , in the mushy zone composed of austenite dendrites and  $\delta$ -ferrite, (b)  $1208^{\circ}\text{C} \pm 15^{\circ}\text{C}$ , partial eutectoid transformation of the  $\delta$ -ferrite into  $\sigma + \gamma_2$ , (c)  $950^{\circ}\text{C} \pm 15^{\circ}\text{C}$ ,  $\delta$ -ferrite is fully transformed into  $\sigma + \gamma_2$ .

### 3.2. Solidification path: comparison between experimental and numerical results

Figure 3 compares the experimental and the numerical solidification path. It was chosen to report the difference between liquidus temperature and considered temperature, due to experimental error made on the temperature measurements in order to compare with ThermoCalc<sup>®</sup> calculations. The numerical path was calculated considering the Gulliver-Scheil model implemented in ThermoCalc<sup>®</sup> software. No diffusion for the substitutional elements and a complete diffusion for the faster elements that are carbon and nitrogen is assumed for the calculations. The numerical solidification interval ( $164^{\circ}\text{C}$ ) is larger than the experimental ( $85^{\circ}\text{C}$ ), this difference can be explained by the hypothesis considered in the Gulliver-Scheil model. There is no back-diffusion and infinite diffusion in the liquid, whereas in real conditions, the elements in the solid diffuse partially during the solidification process and the diffusion in the liquid is finite. An equilibrium calculation considering the lever rule showed that the solidus temperature is  $1276^{\circ}\text{C}$  with a fully austenite microstructure. A diffusion calculation for the Cr, Ni and Mo showed that diffusion length are low in austenite, which indicates that the QDS sample is not too far away from Scheil hypotheses. As a part of future work, the solidification should be described with a diffusion model to improve the comprehension of these results.

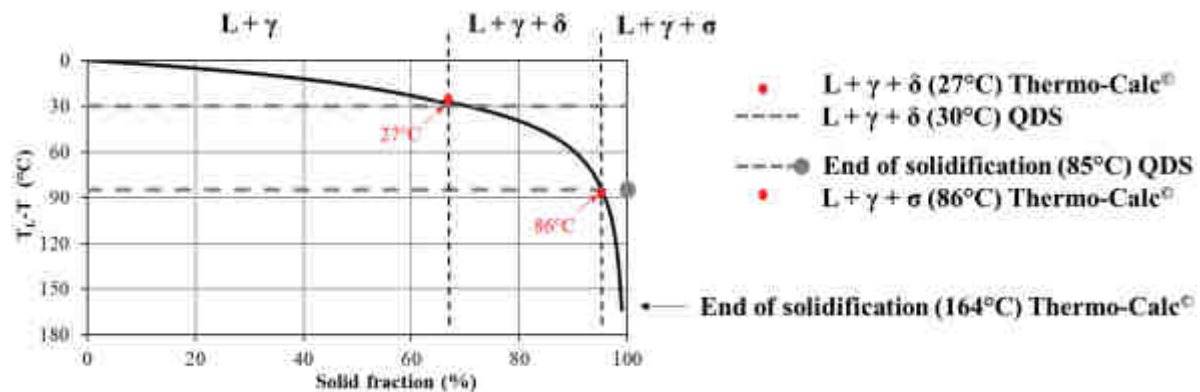


**Figure 3** – Experimental and numerical solidification path

In both experimental results and numerical calculations, the solidification starts with austenite dendrites. 30°C below the liquidus temperature,  $\delta$ -ferrite precipitates in the QDS sample. This value is close to that predicted with ThermoCalc<sup>®</sup> calculations (27°C). The solidification ends at 85°C below the liquidus temperature for the QDS sample. By calculation, the solidification progresses with the  $\sigma$ -phase formation at 86°C below the liquidus temperature and ends 164°C below the liquidus temperature. As a reminder, no  $\sigma$ -phase generated during the solidification process was observed in the QDS sample. This can be explained by the fact that the solidification range is smaller (85°C) in the QDS sample.

#### 4. Conclusion

The solidification path and the solid  $\sigma$ -phase formed during the solidification process of the S31254 alloy were investigated using quenching direction solidification and SEM observations for a cooling rate of 0.5°C/s (1800°C/h). The experimental solidification path was reproduced with ThermoCalc<sup>®</sup> calculations with a good agreement. The solidification process in S31254 steel starts with austenite dendrites and progresses with  $\delta$ -ferrite interdendritic formation due to Mo segregation in the liquid during solidification. The eutectoid decomposition  $\delta \rightarrow \sigma + \gamma_2$  was showed by observations, EDX analysis and literature references. The transformation starts at 1208°C  $\pm$  15°C and ends at 1041°C  $\pm$  15°C when the  $\delta$ -ferrite is completely transformed into  $\sigma + \gamma_2$ . As a part of future work, a QDS sample with a different cooling rate should be carried out on whether, the  $\sigma$ -phase nucleates during the solidification stage. This work should be also followed by crystallographic analysis in order to verify the assumptions made on the nature of the phases.

#### 5. Acknowledgments

The authors would like to thank Industeel and ANRT, which support this work under a CIFRE Ph.D. fellowship (Grant Number 2016-0780).

#### References

- [1] Lai J K L, Shek C H and Lo K H 2012 *Stainless steels: An introduction and their recent developments* (Bentham Science Publishers)
- [2] Stein G, Hucklenbroich I and Feichtinger H 1999 Current and future applications of high nitrogen steels *Materials science forum* vol 318 (Trans Tech Publ) pp 151–160
- [3] Olsson J and Minnich K 1999 Solid stainless steel for MSF once-through plants *Desalination* **124** 85–91
- [4] Koutsoukis T, Redjaïmia A and Fournalis G 2013 Phase transformations and mechanical properties in heat treated superaustenitic stainless steels *Mater. Sci. Eng. A* **561** 477–485

- [5] Machado I F and Padilha A F 2000 Aging behaviour of 25Cr–17Mn high nitrogen duplex stainless steel *ISIJ Int.* **40** 719–724
- [6] Koutsoukis T, Redjaïmia A and Fourlaris G 2011 Characterization of precipitation sequences in superaustenitic stainless steels *Solid State Phenomena* vol 172 (Trans Tech Publ) pp 493–498
- [7] Koutsoukis T, Konstantinidis K, Papadopoulou E G, Kokkonidis P and Fourlaris G 2011 Comparative study of precipitation effects during aging in superaustenitic and superferritic stainless steels *Mater. Sci. Technol.* **27** 943–950
- [8] Lee T-H, Kim S-J and Jung Y-C 2000 Crystallographic details of precipitates in Fe-22Cr-21Ni-6Mo-(N) superaustenitic stainless steels aged at 900 C *Metall. Mater. Trans. A* **31** 1713–1723
- [9] Hsieh C-C and Wu W 2012 Overview of Intermetallic Sigma ( $\sigma$ ) Phase Precipitation in Stainless Steels *ISRN Metall.* **2012**
- [10] Pohl M, Storz O and Glogowski T 2007 Effect of intermetallic precipitations on the properties of duplex stainless steel *Mater. Charact.* **58** 65–71
- [11] Tseng C C, Shen Y, Thompson S W, Mataya M C and Krauss G 1994 Fracture and the formation of sigma phase, M<sub>23</sub>C<sub>6</sub>, and austenite from delta-ferrite in an AISI 304L stainless steel *Metall. Mater. Trans. A* **25** 1147–1158
- [12] Llorca-Isern N, López-Luque H, López-Jiménez I and Biezma M V 2016 Identification of sigma and chi phases in duplex stainless steels *Mater. Charact.* **112** 20–29
- [13] Chen T H and Yang J R 2001 Effects of solution treatment and continuous cooling on  $\sigma$ -phase precipitation in a 2205 duplex stainless steel *Mater. Sci. Eng. A* **311** 28–41
- [14] Perricone M J and DuPont J N 2006 Effect of composition on the solidification behavior of several Ni-Cr-Mo and Fe-Ni-Cr-Mo alloys *Metall. Mater. Trans. A* **37** 1267–1280
- [15] Hsieh C-C, Lin D-Y and Chang T-C 2008 Microstructural evolution during the  $\delta/\sigma/\gamma$  phase transformation of the SUS 309LSi stainless steel after aging under various nitrogen atmospheric ratios *Mater. Sci. Eng. A* **475** 128–135
- [16] Banovic S W, DuPont J N and Marder A R 2002 Dilution and microsegregation in dissimilar metal welds between super austenitic stainless steel and nickel base alloys *Sci. Technol. Weld. Join.* **7** 374–383
- [17] Lacaze J and Lesoult G 1995 Modelling the development of microsegregation during solidification of an Al-Cu-Mg-Si alloy *ISIJ Int.* **35** 658–664
- [18] Anderson T D, Dupont J N, Perricone M J and Marder A R 2007 Phase transformations and microstructural evolution of Mo-bearing stainless steels *Metall. Mater. Trans. A* **38** 86–99
- [19] Kim Y-J, Chumbley L S and Gleeson B 2004 Determination of isothermal transformation diagrams for sigma-phase formation in cast duplex stainless steels CD3MN and CD3MWCuN *Metall. Mater. Trans. A* **35** 3377–3386